V European Conference on Computational Fluid Dynamics
ECCOMAS CFD 2010
J. C. F. Pereira and A. Sequeira (Eds)
Lisbon, Portugal,14-17 June 2010

PROPELLER-FLOW PREDICTIONS USING TURBULENT VORTICITY-CONFINEMENT

Manuel Manzke*, Thomas Rung†

*Hamburg University of Technology - Institute for Fluid Dynamics and Ship Theory,
Schwarzenbergstraße 95(C) - 21073 Hamburg - Germany
e-mail: manuel.manzke@tu-harburg.de
†Hamburg University of Technology - Institute for Fluid Dynamics and Ship Theory
Schwarzenbergstraße 95(C) - 21073 Hamburg - Germany
e-mail: thomas.rung@tu-harburg.de

Key words: Propeller Flow, Turbulent Vortical Flow, Vorticity Confinement, Turbulence Modelling

Abstract. *The paper reports on an attempt towards a turbulent vorticity-confinement strategy for RANS-based industrial propeller-flow simulations. Attention is given to a more rigorous separation between direction, intensity and selectivity of the confinement approach The example included refers to the INSEAN E779a propeller at Re=1.5 10^6, for different advance ratios. The methodology aims at an improved prediction of tip vortices, which are an origin of cavitation. Results indicate the strengths of the rigour approach to perform a dedicated confinement.*

1 INTRODUCTION

The availability of detailed, localised flow information provides an excellent opportunity to optimise the design of marine propellers with respect to cavitation by means of CFD. Cavitating marine-propeller flows are, however, difficult to simulate since they are governed by the influence of turbulence and concentrated vortices, e.g. hub and tip vortices. Both, the predictive effort and the simulation accuracy particularly hinge on a fair simulation of the downstream evolution of primary vortices. Viscous simulation methods are deemed to be afflicted by a prohibitive effort if an adequate resolution of the individual vortex path should be achieved. The problem is particularly severe for industrial-flow simulations, due to the huge computational expenses associated to (locally) refined meshes for flows around complex applications at ship Reynolds numbers around $Re \approx 10^9$. Accordingly, the simulation usually mimics the vorticity only in the vicinity of the shedding origin, e.g. a propeller tip, but fails to track the vortex downstream.

Traditional Boussinesq-viscosity RANS procedures are the most viable and widespread approaches to turbulent industrial flow simulations. The related turbulence closures are however known to introduce an unrealistic amount of vortex-diffusion through an overestimated eddy-viscosity. This motivates the use of a modified computational model based on turbulent vorticity-confinement.

2 NUMERICAL METHOD

The present work is based on the viscous flow simulation suite FreSCo$^+$[10]. The finite-volume RANS-procedure is a spin-off of the FreSCo solver, a joint development of Hamburg University of Technology, the Hamburg Ship Model Bassin (HSVA) and the Dutch Maritime Research Institute (MARIN). The package is supplemented by an adjoint flow solver AD-FreSCo$^+$ (dedicated to optimisation) and an overset-grid technique (OVER-FreSCo$^+$). The original code was developed within the scope of the EU initiative VIRTUE. The procedure uses a segregated algorithm based on the strong conservation form of the momentum equations. It employs a cell-centered, colocated storage arrangement for all transport properties. Structured and unstructured grids, based on arbitrary polyhedral cells or hanging nodes, can be used. The implicit numerical approximation is second-order accurate in space and time. Integrals are approximated using the conventional mid-point rule. The solution is iterated to convergence using a pressure-correction scheme. Various turbulence-closure models are available with respect to statistical (RANS) or scale-resolving (LES, DES) approaches. Two-phase flows are addressed by interface-capturing methods based upon the Level- Set or Volume-of-Fluid (VOF) technique. Since the data structure is generally unstructured, suitable pre-conditioned iterative sparse-matrix solvers for symmetric and non-symmetric systems (e.g. GMRES, BiCG, QMR, CGS or BiCGStab) can be employed. The algorithm is parallelised using a domain-decomposition technique based on a Single Program Multiple Data (SPMD) message-passing model, i.e. each process runs the same program on its own subset of

data. Inter-processor communication employs the MPI communications protocol. Load balancing is achieved using the ParMETIS partitioning software.

3 VORTICITY CONFINEMENT

The basic idea of vorticity confinement is to introduce a synthetic body-force vector f_i to the RHS of the momentum equations, e.g. for an incompressible, single-phase Newtonian fluid

$$\rho \frac{\partial U_i}{\partial t} + \rho \frac{\partial (U_k\, U_i)}{\partial x_k} = -\frac{\partial p}{\partial x_i} + \frac{\partial}{\partial x_k}\left[\mu\left(\frac{\partial U_i}{\partial x_k} + \frac{\partial U_k}{\partial x_i}\right)\right] + b_i \; + \rho\, f_i \; . \tag{1}$$

Here ν denotes to the kinematic viscosity, U_i refers to the cartesian velocity coordinates – or their respective mean values in an Reynolds-averaged approach – and ρ, p represent the fluid density and pressure. Mind, that Einstein's summation convention is used. The term b_i comprises all actual body-forces (e.g. due to gravity: $b_i = -\rho g\, \delta_{i3}$) and potential contributions from a Reynolds-averaging process (i.e. $b_i = -\rho\, \partial(\overline{u_i u_k})/\partial x_k$).

The synthetic body force f_i should neutralise the vorticity change due to an artificial viscosity. The artificial viscosity can either be attributed to discretisation errors and the employed finite-approximation scheme [11] or errors induced by the utilised physical models. An illustrative starting point to motivate the vorticity-confinement is the transport equation for the cartesian coordinates of the vorticity vector ω_k, viz.

$$\omega_k = \epsilon_{kmj}\, \frac{\partial U_j}{\partial x_m} \; ,$$

in an incompressible, laminar, single-phase flow field

$$\frac{D\omega_k}{Dt} = \underline{\left[\frac{\partial}{\partial x_j}\left(\nu \frac{\partial \omega_k}{\partial x_j}\right) + \epsilon_{kji} \frac{\partial (b_i/\rho + f_i)}{\partial x_j}\right]} - \omega_j \frac{\partial U_k}{\partial x_j} \; , \tag{2}$$

where ϵ_{kji} is the permutation tensor. The underlined term is of particular interest. The first part denotes the viscous change of vorticity vector while the second part describes the respective change due to body forces. An appropriate formulation of f_i might reduce the viscous term and thereby remove erroneous viscous diffusion.

Obviously, the introduction of a source term is a manipulation of the momentum equation. Accordingly, different vorticity-confinement strategies focussing upon different error sources are conceivable. As regards the compensation of discretisation errors and modelling errors obtained from filtered (LES) equations, the confinement is only defensible if the manipulation inherently vanishes in the continuous limit. The confinement is thus part of the computational model which consists of the physical model (turbulence model) and the numerical model (discretisation/approximation). With respect to RANS-based simulations of industrial flows using second-order accurate schemes, turbulence-modelling errors often dominate discretisation errors. The present study aims to apply the vorticity-confinement practice to RANS-based Boussinesq-viscosity applications. Accordingly, the confinement strategy should support grid-convergence.

3.1 Previous Confinement Studies

The original formulation of the body forces goes back to Steinhoff and Underhill [11]. The vorticity-stabilising source term consists of the product between a scalar-valued velocity ϵ and a vector-valued reciprocal time scale s_i, viz.

$$f_i = \epsilon s_i \ . \tag{3}$$

The reciprocal time-scale vector is evaluated from the gradient of the vorticity $\eta = \sqrt{\omega_k \omega_k}$

$$s_i = \epsilon_{ijk}\, n_j\, \omega_k \ , \qquad \text{with} \qquad n_j = \frac{\frac{\partial \eta}{\partial x_j}}{\sqrt{\frac{\partial \eta}{\partial x_k}\frac{\partial \eta}{\partial x_k}}} \qquad \text{and} \qquad \eta = \sqrt{\omega_k \omega_k} \ . \tag{4}$$

Mind, that the vector s_i points towards the vortex core, hence forcing vorticity back to the centre as it diffuses away and thereby reducing the shear-layer thickness. The reduction of the shear-layer thickness is an important aspect for the homogenity-driven assessment of the propeller wake field.

To the authors' knowledge, previous studies have been exclusively performed to bias discretisation errors. In the original work, the velocity scale ϵ is assigned to a constant value. Steinhoff and co-workers have outlined that the computed flow fields are not very sensitive to the parameter ϵ in laminar flow or LES computations [3] on predominantly uniform meshes. Disparate findings have been reported by Muruayam et al. [8] and Löhner et al. [13] using inhomogeneous meshes. Although uniform (isotropic) grids of similar edge size might reduce the sensitivity to the velocity scale ϵ, the invariance of the results with a non-invariant (dimensional) parameter is difficult to accept, even when discretisation errors are targeted. A constant velocity scale might cause problems in areas featuring either large variations of vorticity (i.e. boundary layers) or numerical dissipation, e.g. due to large mesh variations. The latter issue gains importance, when inhomogeneous, unstructured meshes are employed and spatial adjustments are required. Suggestions to account for inhomogeneous meshes have recently been published by Butsuntorn and Jameson [2].

3.2 Aims & Objective of the Present Confinement Study

The predictive error and thereby the velocity scale ϵ in equation (3) are controlled by the independent length and time scales of the investigated problem. They involve combinations of both, grid-based discretisation parameters and the flow-field parameters. A restriction to a subset of scaling parameters can be justified if the subset dominates the representation of the target vortices.

Most modern CFD codes are second-order accurate in space and time. Only minor diffusive errors occur in conjunction with these codes by some small amount of controlled artificial diffusion. With respect to travelling vortices, modelling errors dominate

resolution-based discretisation errors in second-order accurate RANS-based Boussinesq-viscosity procedures, which are the workhorses of industrial CFD. Turbulence is known to be very sensitive to deviations from uni-directional shear flow. However, Boussinesq-viscosity models are difficult to sensitise to such situations. Turbulence production is typically associated with strain in a Boussinesq model. Moreover, rotational strain is known to generate more turbulence than irrotational strain, which has prompted a family of stagnation-point correction approaches, e.g. the modification published by Kato and Launder [6]. Some popular algebraic models – such as the Baldwin-Lomax model [1] – explicitly adhere the turbulent viscosity to the local vorticity magnitude. Hence, overestimated diffusivity mainly results from an overpredicted turbulent viscosity.

The present study aims to apply the vorticity-confinement practice to RANS-based Boussinesq-viscosity applications. The confinement operates as a supplement to the turbulence-modelling practice in order to bias known model weaknesses. The predicted physics of a RANS approach should be virtually insensitive to resolution aspects, although the representation of turbulence relies on scalar invariants of flow-field gradients (e.g. state-of-the-art SST, RNG or EASM models) and might thus suffer from a poor resolution. Strictly speaking, the respective scaling parameters should support grid-convergence. The minimum discretisation effort is however not irrelevant, since it must be ensured, that the mesh is able to resolve the kinematics of the target vortices.

3.3 Rationale of the Present Confinement Strategy

To establish a more general – still problem oriented – vorticity-confinement strategy, a sequence of building blocks for the vorticity-confinement formulation is derived. These building blocks refer to the superposition of scalar-valued, non-dimensional filter functions F_φ, a non-dimensional vector V_i^c and a scalar-valued acceleration S_ψ^c. The filter functions locally restrict the confinement from physical arguments and identify the specific vortices that should be stabilized. The vector V_i^c governs the direction of the manipulation. The intensity of the confinement follows from a scalar parameter S_ψ^c. Several options for this parameter, which also supplies the correct dimension $[m/s^2]$, can be considered in order to identify the dominating source of error. Moreover, truly non-dimensional amplitude factors ϵ_ψ can be applied. The respective formulation of the synthetic body force reads

$$f_i = V_i^c \left[\prod_\varphi F_\varphi\right] \left[\max_\psi(S_\psi^c \epsilon_\psi)\right] . \tag{5}$$

Non-dimensional Vectorial Direction

The vector-valued component of the confinement model is in line with the proposal of Steinhoff, though, it is made dimensionless in the present effort

$$V_i^c = \epsilon_{ijk} \left(\frac{\frac{\partial \eta}{\partial x_j}}{\sqrt{\frac{\partial \eta}{\partial x_m}\frac{\partial \eta}{\partial x_m}}\,\eta + \alpha} \right) \omega_k \,. \tag{6}$$

The parameter α denotes a small number to avoid sigularities.

Non-dimensional Scalar Filters

Normalised filter functions $F_\phi \in [0,1]$ are used to exclude non-targeted or include targeted flow regions. An illustrative example refers to the confinement of helical structures. Many vortices of industrial applications are characterised by a significant amount of helicity. Examples refers to tip vortices of a wing/propeller, lee-vortices of trains, aircraft fuselages and submarine hulls. Modifications of the Steinhoff approach which are focussing upon helical structures have been proposed by various authors [2, 9] in conjunction with tip vortices in aeronautical applications. More appropriately, a (high-pass) filter-function identifying the flow regions with strong helicity can be defined by

$$F_h = \frac{\|U_i \omega_i\|}{(\sqrt{U_k U_k})\,\eta + \alpha}\,, \qquad F_h \in [0,1]. \tag{7}$$

The helicity filter looks attractive for most nautical problems like propeller or wake flows, because the crucial primary vortices are often aligned with the velocity vector. If the computational domain is rotating, a slightly modified version for the helicity filter is applied in the present study, viz.

$$F_{hb} = tanh\left(\frac{\|U_{b_i} \omega_i\|}{(\sqrt{U_k U_k})\,\eta + \sqrt{\omega_{b_k}\omega_{b_k}}\sqrt{U_{b_k} U_{b_k}}} \right)\,, \qquad F_h \in [0,1]\,, \tag{8}$$

where U_{b_i} denotes the coordinates moving grid velocity at each cell center and ω_{b_k} the instantaneous rotation vector of the moving grid.

An important aspect is to exclude the viscous boundary-layer regime from the confinement manipulation. Accordingly, appropriate laminar or turbulent (high-pass) filter functions can be borrowed from basic fluid mechanics or turbulence modelling strategies [7], e.g.

$$F_w = tanh\left(\frac{\sqrt{k}\; d_{\mathrm{w}}}{500\nu} \right) \qquad \text{or} \qquad F_w = tanh\left[\left(\frac{d_{\mathrm{w}}}{\frac{5 L_{ref}}{\sqrt{Re}}} \right)^5 \right]\,, \qquad F_w \in [0,1]\,. \tag{9}$$

Here, k denotes the turbulent kinetic energy, d_w the wall distance, L_{ref} an external reference length (e.g. the blade chord) and Re the Reynolds number.

Another attempt might be to restrict the influence of the vorticity confinement to vortices of a known origin. This can be realised using the λ_2-criterion of Jeong and Hussain [5]. The identification of a vortical region can be obtained from analysing the (negative) second largest eigenvalue λ_2 of the symmetric tensor $S_{ij}^2 + W_{ij}^2$. Unfortunately, the specific value to be tracked is not apriori known. It can, however, be computed from the λ_2-value found at a location, which is known to be part of the vortex (e.g. in the tip region). The respective (digital) filter reads

$$F_{\lambda_2} = \begin{cases} 1 & , \lambda_2 \leq \overline{\lambda}_2 \\ 0 & , \lambda_2 > \overline{\lambda}_2 \end{cases} . \tag{10}$$

Mind, that the tracked (negative) $\overline{\lambda}_2$-value is not uniquely aligned to a specific vortex and the filter might thus be ineffective for multiple vortical regimes.

Further application-oriented physical and geometrical filter operations – e.g. with respect to vortex stretching – can be formulated.

Scalar Amplitude

The scalar-valued acceleration, which has been used by Butsuntorn and Jameson [2] for laminar flow computations reads

$$S_v^c = \sqrt{U_i U_i}\, \eta \, , \quad \text{with} \quad \epsilon_v = 0.035 - 0.075 \, . \tag{11}$$

This vorticity-confinement formulation does not inhere any grid information and does not vanish in the continuous limit. As alluded to before, the evolution of vortices in RANS simulations using Boussinesq-viscosity closures, is often impaired by excessive levels of turbulent viscosity. The latter is due to the inability of the isotropic closure to mimic the influence of streamline curvature, particularly in conjunction with turbulence-attenuating, positive curvature. To address this phenomenon, one can utilize a scalar-valued parameter which identifies regions with combinations between high values of turbulent viscosity and vorticity changes. Various options exist in accord with the traditional approach outlined in equation (11). One option directly employs the eddy viscosity, e.g. for a $k-\omega$ or a $k-\epsilon$ model,

$$S_{t1}^c = \nu_t \sqrt{\frac{\partial \eta}{\partial x_k}\frac{\partial \eta}{\partial x_k}} \approx Tu \left(\frac{\sqrt{k}\sqrt{\frac{\partial \eta}{\partial x_k}\frac{\partial \eta}{\partial x_k}}}{\eta \omega} \right) \sqrt{U_i U_i}\, \eta \approx Tu \left(\frac{k^{3/2}/\varepsilon \sqrt{\frac{\partial \eta}{\partial x_k}\frac{\partial \eta}{\partial x_k}}}{\eta c_\mu} \right) \sqrt{U_i U_i}\, \eta \, . \tag{12}$$

A more simple alternative sceens for regions with high turbulence intensity Tu, viz.

$$S^c_{t2} = \left(\frac{\sqrt{k}}{\sqrt{U_m U_m}} \right) \sqrt{U_i U_i} \eta \approx Tu \, \sqrt{U_i U_i} \, \eta \; . \tag{13}$$

Mind, that the turbulence intensity is usually significantly smaller than one. The inclusion of the turbulence intensity provides an inhomogeneous, non-dimensional amplification factor. In an engineering shear flow Tu is in the range of 1% – 10% and one recovers amplitude values close to the above mentioned values communicated by Butsuntorn and Jameson. Moreover, S^c_{t2} usually exceeds S^c_{t1} in RANS simulations.

The rationale can also be extended to scale-resolving LES or DES approaches if confined to modelling errors. Accordingly, one should note, that the turbulent viscosity of the LES regime scales with the square of the a local grid-spacing measure h, viz.

$$\nu_t \approx \eta \, (0.2 \, h)^2 \, , \quad \text{thus} \quad S^c_{t1} = \eta \, (0.2 \, h)^2 \, |\underline{\nabla} \eta| \; ,$$

which is agrees approximately with Löhner et al. [13] for $\epsilon_{t1} \approx 5$. However, with an increase of the physical resolution capabilities, discretisation aspects might become more important for the error in equation (2).

Another option for S_c can be derived from the transport equation of the enstrophy η^2

$$\frac{D\eta^2}{Dt} = \nu \frac{\partial^2 \eta^2}{\partial x_i^2} + 2\omega_i \omega_k \frac{\partial U_i}{\partial x_k} - 2\nu \frac{\partial \omega_i}{\partial x_k} \frac{\partial \omega_i}{\partial x_k} \, ,$$

whose last term describes the viscous dissipation of vorticity. Accordingly, an amplitude parameter reads

$$S^c_h = 2 \frac{\nu}{\eta^3} \, \frac{\partial \omega_j}{\partial x_k} \frac{\partial \omega_j}{\partial x_k} \, \sqrt{U_i U_i} \, \eta \; . \tag{14}$$

More alternatives for the definition of S^c can bederived, e.g. the ratio of the convective time-scale to the rotational time-scale or grid-based approaches [13].

Amplitude Parameter

Ideal amplitude parameters ϵ_ψ would remove all erroneous vortex-diffusion, originating from grid and model errors. Accordingly, intensive grid-convergence and sensitivity studies should be performed, which is beyond the scope of the present paper. We thus restrict ourselves to small variations of ϵ_ψ around the unity value.

4 APPLICATION EXAMPLE

The present vortex confinement strategy is applied to the simulation of the INSEAN E779a propeller, for which an experimental analysis has been performend at INSEAN in a non cavitating flow regime [4]. Experiments were conducted in a closed-circuit tunnel with

a square-shaped test section. The propeller is a simple, four-bladed Wageningen modified type, skewed propeller with uniform pitch ($\frac{P}{D} = 1.1$). It has a diameter of $D = 0.2272m$ and a chord length of $0.086m$ at $\frac{r}{R} = 0.7$. To obtain an open-water curve, thrust and torque of the propeller have been measured for several advance ratios

$$J = \frac{U_\infty}{nD}. \tag{15}$$

The propeller revolution rate was kept constant at $n = 36s^{-1}$, while the tunnel velocity U_∞ has been varied to achieve different advance ratios. Table 1 summarizes the inflow velocities, and the respective Reynolds numbers based on the chord length at $r/R = 0.7$ for the simulated advance ratios.

$n[Hz]$	J	$U_\infty[m/s]$	$Re_{0.7}$
36.03	0.65	5.3225	$1.455 \cdot 10^6$
36.02	0.71	5.8122	$1.466 \cdot 10^6$
36.02	0.771	6.3116	$1.478 \cdot 10^6$
36	0.83	6.7908	$1.490 \cdot 10^6$
36	0.879	7.1917	$1.501 \cdot 10^6$

Table 1: Approach-flow conditions for the investigated advance ratios.

The present research is devoted to a typical industrial CFD setup. The employed numerical grid is depicted by Figure 2. The grid consists of approximately 1 million control volumes and utilises local refinement. Wall functions have been used to mimic the near-wall turbulence behaviour with $y^+ \approx 30$. The simulations are performed in an

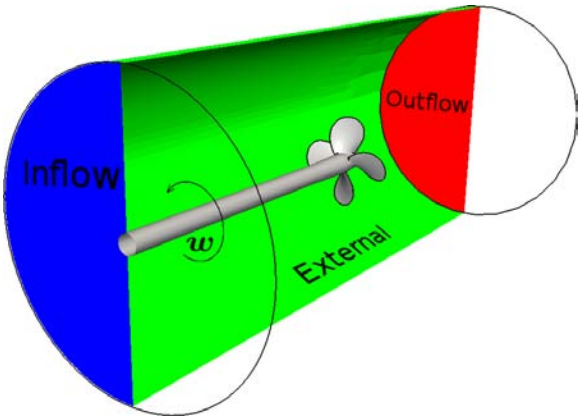

Figure 1: Illustration of the computational domain.

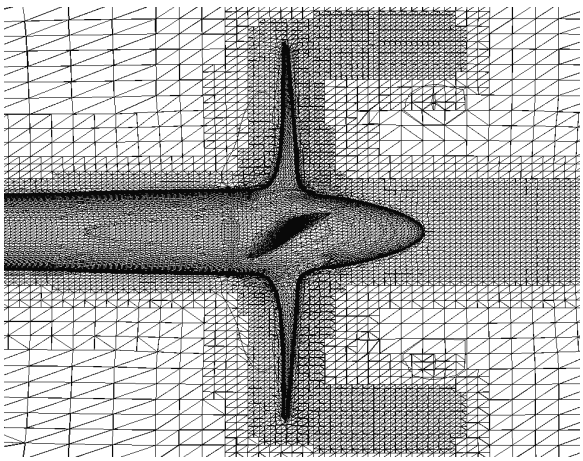

Figure 2: Grid near the propeller.

inertial frame of reference. The computational domain is rotating at the revolution rate of the experimental setup. A uniform velocity is prescribed at the inflow boundary. Along

the outer circumference (labeled "External" in Figure 1), a slip-wall boundary condition has been applied. At the outflow a uniform pressure is imposed. Turbulence has been modelled with the Wilcox $k-\omega$ turbulence model [12].

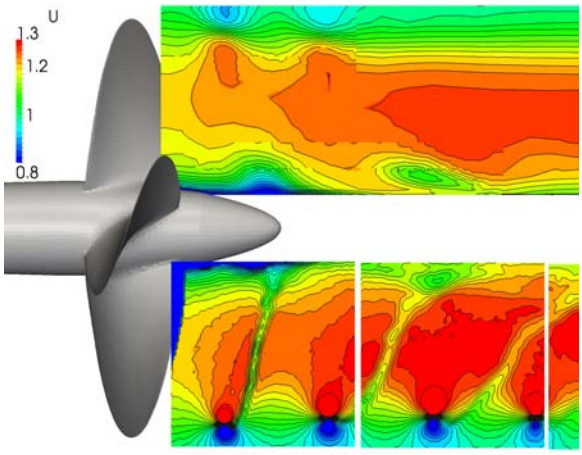

Figure 3: Comparison of predicted normalized axial-velocity contours for $J = 0.879$ (top) and experimental data (bottom) for a baseline simulation without vorticity confinement.

Emphasis of the experimental work is given to $J = 0.879$, where detailed Particle-Image-Velocimetry (PIV) and Laser-Doppler-Velocimetry (LDV) measurements are available. Accordingly, a standard RANS-simulation without confinement is performed for this advance ratio to identify the predictive weaknesses of the initial state. Figure 3 compares the axial velocities obtained from PIV measurements displayed in the bottom with simulation results displayed in the top. At small radii and near the hub, the simulation compares favourably with the experiments. On the contrary, the tip-vortex predicition is afflicted by the previously described eddy-viscosity driven vortex-diffusion. To counteract the rapid dissipation of the tip vortex, vorticity confinement will be applied to the simulation henceforth.

Mind, that a clear footprint of the propeller-blade pass is visible in the experimental data between the tip and the hub region. This footprint is hardly visible in the simulation results. However, the footprint consists of small structures and the mesh resolution is deemed inadequate to resolve these structures.

4.1 Applied Confinement Strategy

Assuming the turbulence-modelling error to dominate the discretization error, we restrict ourselves to the scalar amplitude S^c_{t2}. As indicated by Figure 4, this choice yields undesirable confinement contributions within the boundary-layer region. To exclude the boundary layer from the vorticity confinement, we employ the wall filter F_w which is illustrated in Figure 5. The result of the combined application of S^c_{t2} and F_w is depicted by Figure 6. Simulations with different amplitude parameters ϵ_ψ have been performed at

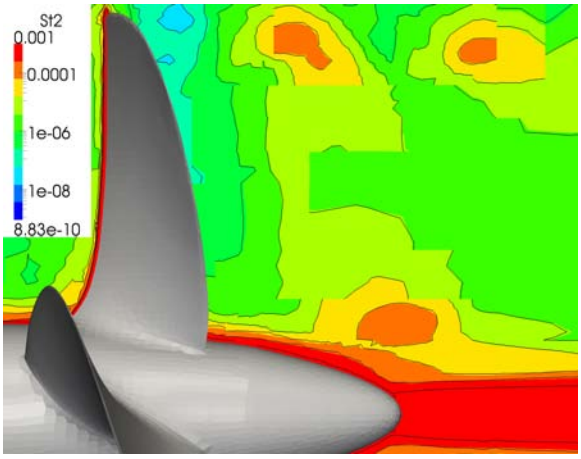

Figure 4: Contourplot of the employed amplitude S^c_{t2} normalized with its maximum.

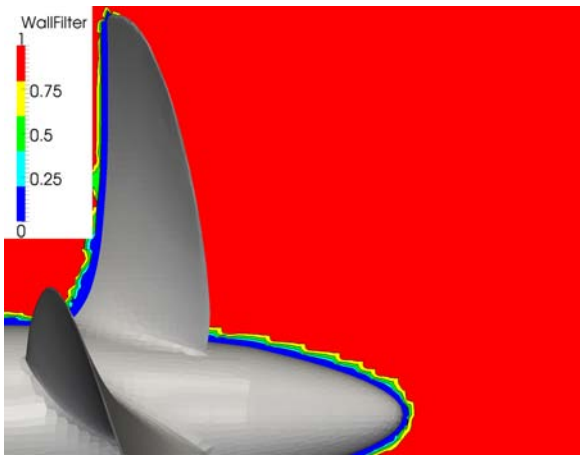

Figure 5: Contourplot of the employed wall filter F_w.

$J = 0.879$ for the source term f_{WT_i}, which reads

$$f_{WT_i} = \epsilon_\psi \, (F_w \, S^c_{t2} \,) V^c_i \; .$$

As displayed by Figure 6 all primary vortices are detected. Mind the log-scaling used in Figure 6. The confinement source drops to zero in the boundary layer and the maximum source is located in the hub-vortex area. In the tip-vortex regime, only minor contributions are observed. Due to the large turbulence intensity, the confinement source is two orders smaller in the tip-vortex region, than in the hub-vortex region.

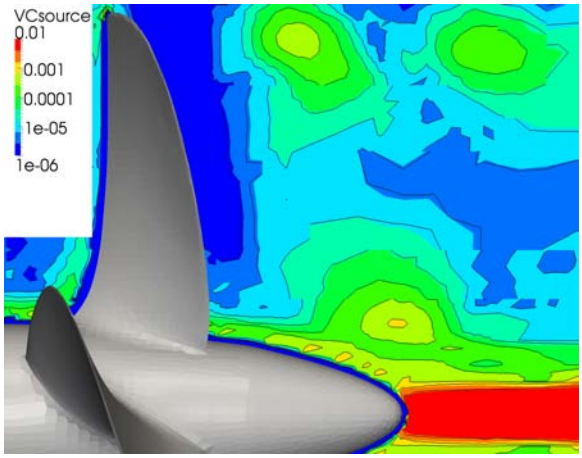

Figure 6: Vorticity confinement (f_{WT_i}); Magnitude of the source term f_{WT_i} normalized with its maximum.

Stable and converging simulation were restricted to $\epsilon_\psi \leq 1$. Unfortunately, the simulation performed with $\epsilon_\psi = 1$ reveals bigger discrepancies in the hub-region compared to the experiment, than the simulations without confinement (cf. Figure 7). It can be observed,

that the flow in this region is erroneously accelerated due to the confinement. Although the tip vortices are augmented, there is still a severe deviation from the experimental results.

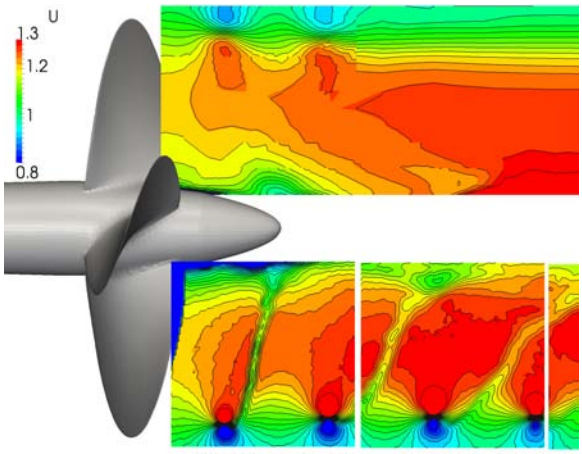

Figure 7: Simulations with vorticity confinement (f_{WT_i}); Comparison of computed normalized axial-velocity contours (top) for $J = 0.879$ against experimental data (bottom).

In order to improve the confinement strategy, an additional filter which excludes the hub region is desirable. Moreover, a higher amplitude parameter ϵ_ψ seems necessary to obtain a better representation of the tip vortices. The non-dimensional helicity filter F_{hb} for rotating grids displayed in Figure 8 is used to supress the confinement in the hub regime. The filter clearly detects the tip vortices and is close to zero in the hub region. Including F_{hb} to the previously described confinement strategy, we arrive at

$$f_{WTH_i} = F_{hb}\, f_{WT_i} = \epsilon_\psi \, (F_{hb}\, F_w\, S^c_{t2}\,) V^c_i \; .$$

The resulting magnitude of the source term is shown in Figure 9. It is seen, that the magnitude of the source term in the tip-vortex region is of the same size as the source term in the hub-vortex region. Due to the more restrictive filtering, a higher amplitude parameter of $\epsilon_\psi = 5$ is applicable. Results of the simulation using f_{WTH_i} together with $\epsilon_\psi = 5$ are shown in Figure 10. Compared to the simulation with f_{WT_i}, the tip vortices show an additional backing. At the inner radii, results outperform the predictions obtained from f_{WT_i}, but are still inferior to the simulations without confinement.

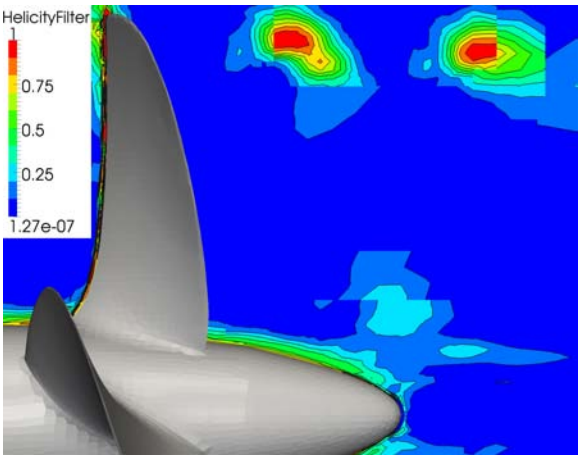

Figure 8: Contourplot of the helicity filter F_{hb}.

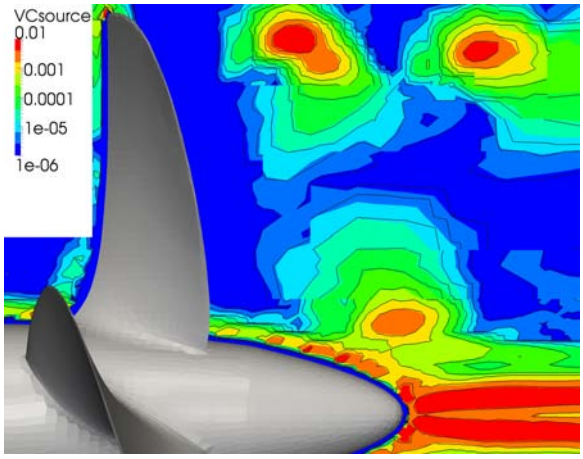

Figure 9: Vorticity confinement (f_{WTH_i}); Magnitude of the source term f_{WTH_i} normalized with its maximum.

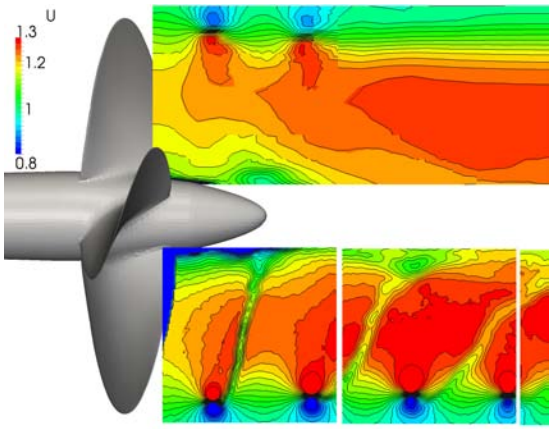

Figure 10: Simulations with vorticity confinement (f_{WTH_i}); Comparison of computed normalized axial-velocity contours (top) for $J = 0.879$ against experimental data (bottom).

4.2 Results for Different Advance Ratios

The subsection is devoted to a direct comparison of results achieved with and without confinement for different operating points of the propeller. The comparison is based upon an observation of iso-surfaces of the vorticity magnitude. The observed value is assigned to $\sqrt{\omega_k \omega_k} = 500$ and represents the vortices originating from one blade. The latter is more illustrative as a corresponding λ_2 iso-surface as it is subjected to a stronger diffusion. The iso-surfaces are coloured with the pressure coefficient

$$-0.2 \leq \; C_p = \frac{p - p_\infty}{0.5\rho(nD)^2} \; \leq 0.2$$

to judge the efficiency of the confinement. Within the region of the tip vortices, five slices at different x-positions are shown.

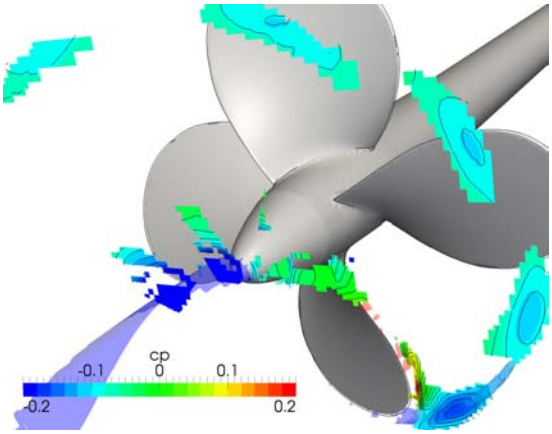

(a) Simulation without confinement; Vorticity iso-surface coloured by Cp.

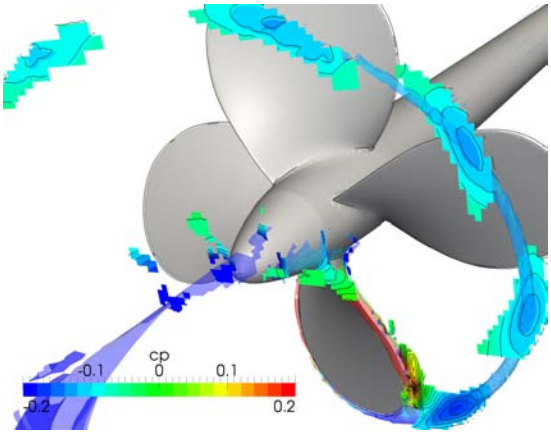

(b) Simulation with f_{i_1} confinement; Vorticity iso-surface coloured by Cp.

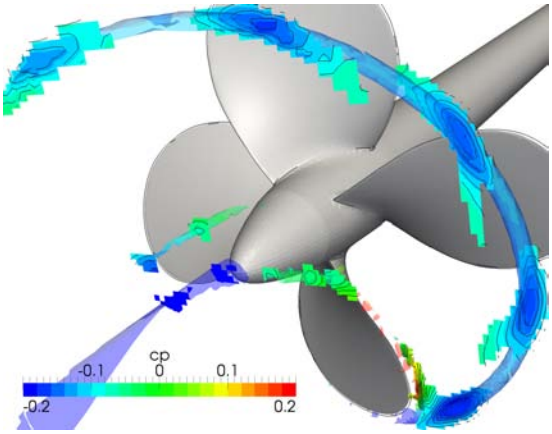

(c) Simulation with f_{i_2} confinement; Vorticity iso-surface coloured by Cp.

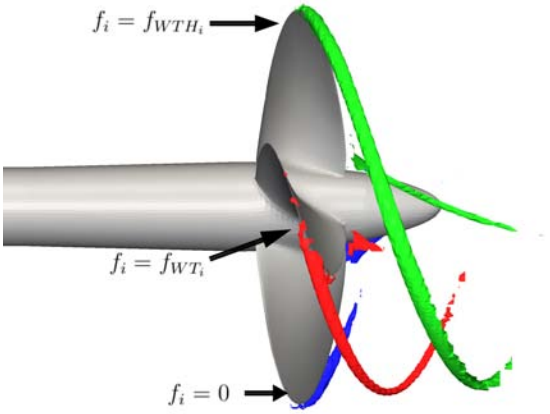

(d) Comparison of iso-surfaces for the different approaches.

Figure 11: Coloured iso-vorticity surfaces ($\sqrt{\omega_k \omega_k} = 500$) for different simulation approaches at $J = 0.879$.

As indicated by Figure 11(a), the leading-edge vortex dissipates quickly without vortex confinement. Accordingly, the pressure minimum, which coincides with a vortex core, also increases rapidly along the vortex path.

Applying the confinement source f_{WT_i} with $\epsilon_\psi = 1$, the dissipation of the vortex is reduced in accord with a slower increase of the pressure minimum (cf. Fig. 11(b)). The pressure increase along the vortex path is still overpredicted. On the trailing edge of the blade an influence of the confinement is observed.

Figure (11(c)) displays the results for the simulation employing f_{WTH_i} in conjunction with $\epsilon_\psi = 5$. The trailing edge vortices start to dissipate in the region where the mesh resolution gets inadequate. The local pressure minimum stays almost constant but might still be overestimated. At the root of the propeller blade, a second vortex can be clearly seen, which is hardly visible in the other simulations.

Figure 11(d) shows the vortices originating from the trailing edge and the propeller blade root. The hub vortex is not shown for sake of clarity. Employing vorticity confinement, the vortex path can be tracked for much longer distances. Additionally, small-scale structures like the vortex originating from the propeller blade root, become visible. The diameter of the vortex tube is increasing, which reveals higher vorticity magnitudes in the center.

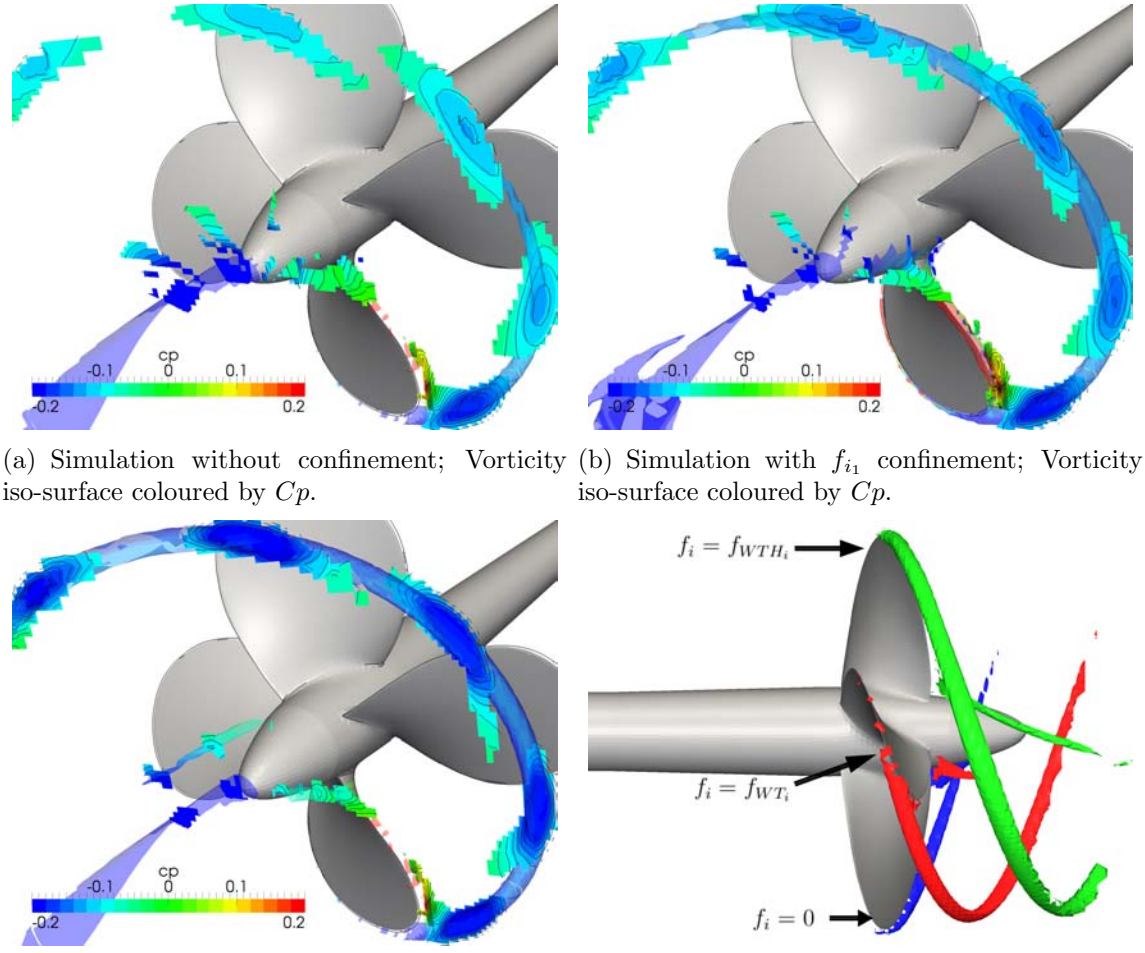

(a) Simulation without confinement; Vorticity iso-surface coloured by Cp.

(b) Simulation with f_{i_1} confinement; Vorticity iso-surface coloured by Cp.

(c) Simulation with f_{i_2} confinement; Vorticity iso-surface coloured by Cp.

(d) Comparison of iso-surfaces for the different simulation approaches.

Figure 12: Isosurfaces of $\sqrt{\omega_k \omega_k} = 500$ for different simulation approaches at $J = 0.83$.

Reducing the advance ratio, increases the angle-of-attack for the propeller blades. Thereby, a higher thrust is achieved and stronger vortices shed from the propeller blades. This can be seen in Figure 12(a), where the result of the simulation without confinement is shown for $J = 0.83$. Using the same iso-value of the vorticity magnitude, the vortex path of the leading-edge vortex is longer than for $J = 0.879$. However, strong dissipation and

the associated increase of the local pressure minimum are again observed. Applying the vorticity confinement f_{WT_i} (cf. Figure 12(b)) and respectively f_{WTH_i} (cf. Figure 12(c)) reveals the same tendencies as for $J = 0.879$. The first choice strengthens the vortex and thereby prolongs the visible path length, but still too much dissipation is found. For the second variant, the vortex starts to dissipate when the mesh resolution deteriorates. The comparison of the results achieved with the different simulations in Figure 12(d) indicates that the path lengths of the trailing edge vortices achieved with the simulations utilizing vorticity confinement are nearly similar. However the strength of the vortices indicated by the diameter of the iso-surface tube are different. As it has been observed for $J = 0.879$ a small vortex originating from the propeller blade root, is only visible using f_{WTH_i}. The

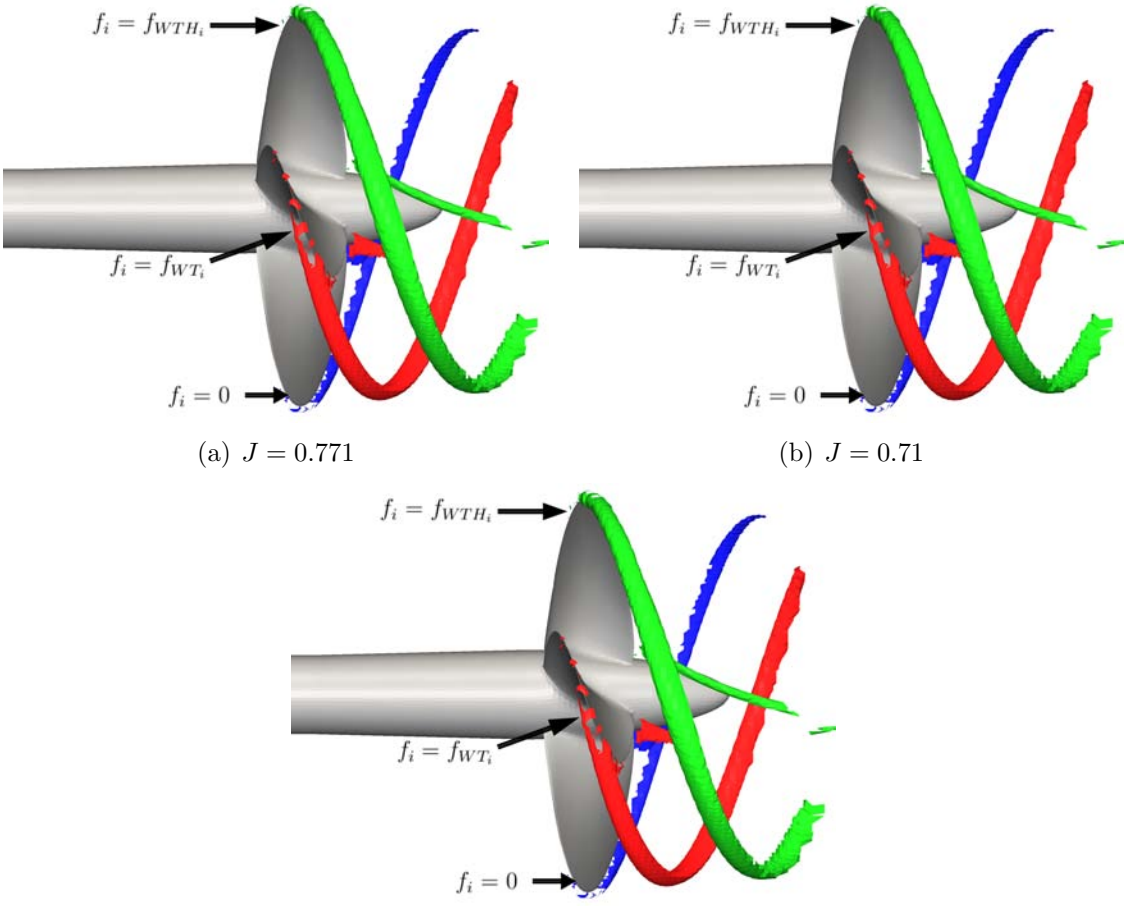

(a) $J = 0.771$ (b) $J = 0.71$

(c) $J = 0.65$

Figure 13: Isosurfaces of $\sqrt{\omega_k \omega_k} = 500$ for different simulation approaches at various J.

findings observed for simulations at $J = 0.879$ and $J = 0.83$ are confirmed by other advance ratios. The influences of the applied confinement strategies on the primary vortices are depicted in Figures 13(a) to 13(c) for $J = 0.771$, $J = 0.71$ and $J = 0.65$.

4.3 Open-Water Diagram

Integral values of thrust and torque are presented in non-dimensional values by means of

$$k_t = \frac{T}{\rho n^2 D^4} \qquad \text{and} \qquad k_q = \frac{Q}{\rho n^2 D^5} \tag{16}$$

where T denotes the thrust and Q being the torque. The open-water diagrams shown in Figure 14 to 16 show the thrust and torque coefficients over the advance ratio. Additionally the effeciency coefficient

$$\eta = \frac{J}{2\pi}\frac{k_t}{k_q} \tag{17}$$

is shown.

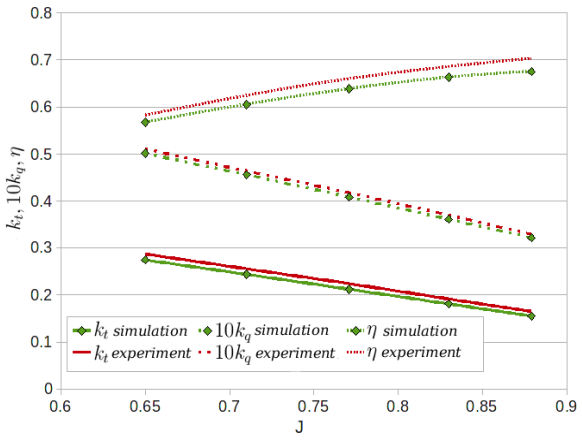

Figure 14: Open-water diagram for simulations without confinement.

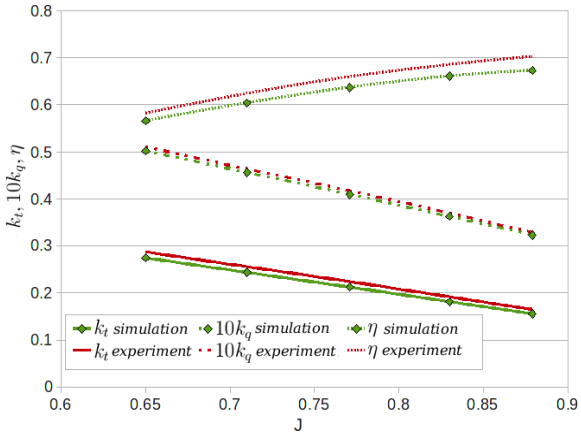

Figure 15: Open-water diagram for simulations using f_{WT_i}.

Figure 14 refers to the predicted open-water diagram for the simulations without vorticity confinement. A slight underestimation of the measured values of k_t and k_q is observerd over the whole range of simulated advance ratios J. As indicated by the underpredicted efficiency, the underprediction of the thrust coefficient is larger than the underprediction of the torque coefficient. The latter can be due to the misrepresentation of the exact tunnel geometry. Applying vortex confinement, only minor influences on the thrust and torque coefficients can be observed. As indicated by Figures 15 and 16, the maximum deviation is less than half a percent.

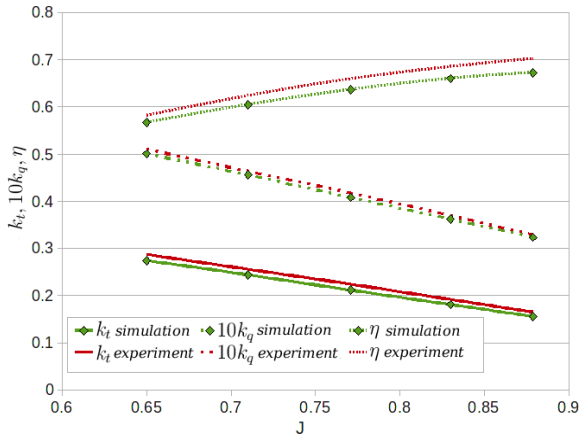

Figure 16: Open-water diagram for simulations using f_{WTH_i}.

5 CONCLUSION

A more rigorous approach to derive vorticity-confinement formulations has been discussed. The latter strictly separates between direction, intensity and filtering/selectivity aspects. The approach has been used to derive a turbulent vorticity-confinement formulation.

The performance of the methodology has been scrutinized for propeller flow applications at different advance ratios using two different filtering techniques. Using turbulent vorticity confinement in conjunction with RANS-based methods, more accurate tip-vortex predictions can be obtained on relatively coarse grids. However, the attainable accuracy and robustness of the RANS-based vortex-confinement approach still hinges significantly on an appropriate filtering.

REFERENCES

[1] B. Baldwin and H. Lomax. Thin-layer approximation and algebraic model for separated turbulent flows. *AIAA Paper 1978-0257*, 1978.

[2] Nawee Butsuntorn and Antony Jameson. Time Spectral Method for Rotocraft Flow with Vorticity Confinement. *AIAA Paper 2008-7340*, 2008.

[3] W. Dietz, G. Hu C., C. Braun, J. Steinhoff, Y. Wenren, M. Fan, and B. Grossman. Efficient eulerian computation of realistic rotorcraft using vorticity confinement: A survey of recent results. *AIAA Paper 2001-0996*, 2001.

[4] G.Calcagno, F. Di Felice, M. Felli, S. Franchi, F.Pereira, and F.Salvatore. The INSEAN E779a Propeller Test Case: a Database for CFD validation. In *MARNET-CFD Final Workshop*, 2003.

[5] J. Jeong and F. Hussain. On the identification of a vortex. *J. Fluid Mechanics*, 285:69–94, 1995.

[6] M. Kato and B.E. Launder. The modeling of turbulent flow around stationary and vibrating square cylinders. *Ninth Symposium on Turbulent Shear Flows, 1993*, pages 10.4.1–10.4.6, 1993.

[7] F. Menter, M. Kuntz, and R. Langtry. Ten Years of Industrial Experience with the SST Turbulence Model. In *4th Int. Symp. Turbulence, Heat Mass Transfer*, pages 625–632, Egell House, New York, 2003.

[8] S. Obayashi, M. Murayama, and K. Nakahashi. Numerical simulation of vortical flows using vorticity confinement coupled with unstructured grid. *AIAA Paper 2001-0606*, 2001.

[9] M. Robinson. Application of Vorticity Confinement to Inviscid Missile Force and Moment Prediction. *AIAA-Paper 2004-0717*, 2004.

[10] T. Rung, K. Wöckner, M. Manzke, J. Brunswig, C. Ulrich, and A. Stück. Challenges and Perspectives for Maritime CFD Applications. In *Jahrbuch der Schiffbautechnischen Gesellschaft, 103. Band*. Schiffbautechnische Gesellschaft e.V., 2009.

[11] J. Steinhoff and D. Underhill. Modification of the Euler Equations for "Vorticity Confinement": Application to the computation of interacting vortex rings. *Physics of Fluids*, 6:2738–2744, 1994.

[12] D. C. Wilcox. *Turbulence Modelling for CFD. 2nd Ed.* DCW Industries Inc., 2004.

[13] C. Yang, R. Löhner, and R. Roger. Tracking vortices over large distances using vorticity confinement. In *24th Symp. on Naval Hydrodynamics*, 2002.